Adaptive Friction-based Inchworm-like Locomotion

Jiří Kubík Jan Faigl

***Abstract*— In this paper, we study adaptive locomotion for inchworm-like robots that move using friction-based pads inspired by snake scales. The robot moves by alternating extension and contraction phases, which require enough friction at the rear and front pads. Locomotion speed depends on how far the body extends, but it is limited by the friction available on the pads. Since the pads are passive, friction can only be controlled by shifting body weight onto them. The challenge is to balance friction and extension length to achieve fast movement on different terrains. Previous work relied on offline tuning for specific terrain types. We propose a new adaptive controller that automatically adjusts the friction requirements by detecting slippage. We demonstrate the approach using a six-degree-of-freedom inchworm-like robot and three locomotion strategies adapted from the literature, which were tested across four terrain types. The locomotion performance is measured by the achieved average locomotion speed, cost of transport, and reliability. Based on the experimental results, the proposed adaptive locomotion achieves performance similar to offline-tuned locomotion and even surpasses it on certain terrains.**

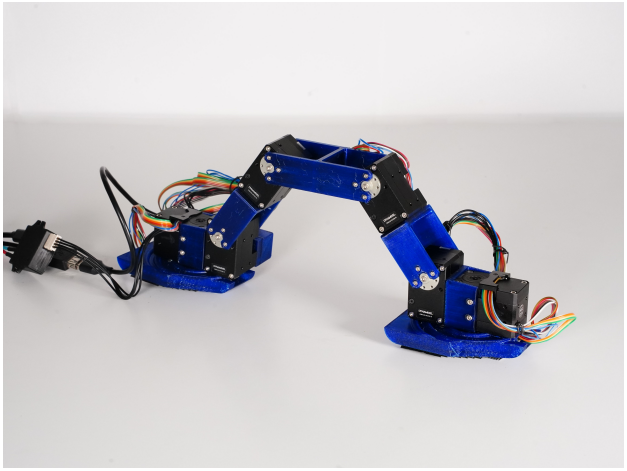

Fig. 1: The designed robot resembles an inchworm and uses anisotropic friction pads with flexible scales for anchoring instead of the limbs found in its biological original.

I. Introduction

Frictional anisotropy allows biological systems to locomote when surfaces generate different friction forces depending on direction. For example, snake-like creatures rely on differences in abdomen scales friction, where the forward direction has lower friction than the backward direction [1]. Inchworm-like locomotion combines this principle with alternating body extension and contraction. Unlike snakes, which generate smooth undulatory gaits, inchworms use their front and rear segments as anchor points, looping the body forward to progress step by step. The locomotion is thus similar to that of legged animals, with alternating phases following repeated motion patterns called *gaits*. In robotics, inchworm-inspired designs have been applied to inspection tasks, using magnets, suction, or bristles to provide anchoring [2]–[6].

Another approach is to exploit materials or structures with anisotropic friction, eliminating the need for specialized anchoring mechanisms [7], [8]. In [9], the authors present an affordable, fully 3D-printable inchworm-like robot with artificial, also 3D printed, scales, which provide sufficient anisotropic friction to locomote the robot forward or backward. A key challenge in such friction-based inchworm locomotion is balancing the anchoring force with the body's extension distance. The robot has to apply sufficient load on the rear pad during extension (and on the front pad during contraction) to prevent slipping. However, prolonging the extension step increases locomotion speed only if sufficient friction is maintained. Since the friction pads are passive, the only way to increase friction is to redistribute body weight. It creates a tradeoff that longer extensions improve speed but risk slippage if the friction is insufficient for the terrain.

Although the work [9] presents an inchworm-like robot capable of locomotion using three gaits, its motion is limited to crawling in 1D, forward and backward. Furthermore, the locomotion parameters are tuned offline for specific surfaces that require prior knowledge of the terrain and are not adaptable to changing environments. We propose addressing these limitations with a novel adaptive locomotion controller that automatically adjusts friction demands based on online slippage detection. Leveraging the approach by the authors of [9], we also employ 3D-printed anisotropic friction pads, but increase the number of *Degrees of Freedom* (DoF) to allow the robot to turn. Besides, we added optical sensors to close the feedback loop, enabling it to adapt its gait parameters in real time, based on slippage detection.

The developed adaptive friction-based locomotion is experimentally validated on an inchworm-like robot depicted in Fig. 1. The robot features 6-DoF and supports three inchworm-inspired locomotion strategies, extended with slippage-aware adaptation and turning. We evaluate the approach across four terrain types and compare it with locomotion tuned explicitly for each terrain, as presented in [9]. Experimental results support the feasibility of an adaptive locomotion controller that achieves performance

The authors are with the Faculty of Electrical Engineering, Czech Technical University, Technická 2, 166 27 Prague, Czechia. {kubikji2, faiglj}@fel.cvut.cz

The presented work was supported by the Technology Agency of the Czech Republic under project No. TN02000028. The research activities of the second author were also supported by the European Union under the project ROBOPROX – Robotics and advanced industrial production (reg. no. CZ.02.01.01/00/22_008/0004590).

similar to offline tuning and even surpasses it in some cases, offering a more robust strategy for friction-based inchworm locomotion.

The remainder of the paper is organized as follows. A brief overview of the related work on slippage detection is presented in the following section. The former inchworm-like locomotion gaits by the authors of [9] are described in Section III to make the paper self-contained. A summary of the new robot design that allows for turning and slippage detection is in Section IV. The proposed generalization of the gaits to turning and adaptive locomotion is presented in Section V. Results on the experimental deployment and achieved robot performance are reported in Section VI. Concluding remarks are summarized in Section VI.

II. Related Work

The related slippage detection is briefly examined in the context of foot slippage affecting the multi-legged robot's posture and stability, and in grasping tasks, where slippage detection enables efficient and adaptive object handling. Multi-legged robots use proprioception to detect slippage, as done by M. Fochhi *et al.* in [10] using foot velocity, by Z. Yoon *et al.* in [11] using both foot velocity and acceleration, or by J. Yang *et al.* in [12] using the *Inertial Measurement Unit* (IMU) and foot velocity. Though the proposed robot locomotion is similar to walking, its slippage lacks the dynamics usually associated with the walking slippage. Nevertheless, measuring foot velocity is crucial for detecting slippage.

On the other hand, slippage detection in grasping tasks uses a wide range of sensors [13], ranging from multi-axial force/torque sensors [14] measuring tangential and normal forces, to force-sensitive resistor (FSR) [15], to specialized piezoresistive nanomaterials [16]. Moreover, the optical sensors are used in the form of elastic elements with markers that deform during grasping, such as GelSight [17], where random markers placed on a flat elastomer are tracked, and TacTip [18], where markers situated on a rubber-like hemisphere are tracked. Notably, Maldanado *et al.* in [19] use the high-speed 30×30-pixel cameras mounted on a robotic hand to track the displacement of a grasped object.

Application of direct optical displacement sensing (akin to an optical computer mouse) in mobile robot locomotion can be limited by the strict requirement for a constant, small distance from the surface, with notable exception of D.-H. Yi *et al.* in [20] that use an afocal optical flow sensor for slippage-invariant odometry on indoor slippery terrain. Building on these optical flow principles and the sensing methods used in robotic grasping, we propose using optical sensing to detect slippage of the inchworm's foot pad. Since inchworm locomotion involves sliding legs against a surface, with the anchoring pad expected to remain stationary, the most suitable location for the sensor is directly on the friction pad. Therefore, we employ a displacement sensor, such as those commonly found in optical or laser mice.

III. Inchworm Robot with 1D Locomotion Gaits

An inchworm-like robot with 3D printed anisotropic friction pads is introduced in [9]. The robot has 4 DoF and is restricted to 1D locomotion (forward or backward). In addition to the robot itself, three locomotion gaits have also been presented. The gaits are tuned offline to enable the robot to locomote on surfaces with different friction levels using keyframe interpolation. All gaits rely on alternating between a support state, in which a segment anchors the robot to the terrain through high static friction, and a slide state, in which the segment's friction is minimized to allow displacement. Since the proposed adaptive locomotion builds on these gaits, they are briefly summarized in the following parts to make the text self-contained.

A. Sliding Gait

Sliding gait implements a straightforward approach to locomotion via two gait phases: *extension* and *contraction*. During the *extension* phase, the distance between contact segments uniformly increases from $l_{\text{min}}^{\text{sliding}}$ to $l_{\text{max}}^{\text{sliding}}$ while the friction pads are aligned to the surface and both contact segments are loaded equally. In the *contraction* phase, the distance decreases from $l_{\text{max}}^{\text{sliding}}$ to $l_{\text{min}}^{\text{sliding}}$. The distance between $l_{\text{min}}^{\text{sliding}}$ and $l_{\text{max}}^{\text{sliding}}$ is referred to as *step length*. Since both segments are equally loaded as outlined in Fig. 2, only the friction pad directional anisotropy is used.

(a) Extension. (b) Contraction.

Fig. 2: Sliding gait phases for $l_{\text{min}}^{\text{sliding}} = 100\,\text{mm}$ and $l_{\text{max}}^{\text{sliding}} = 290\,\text{mm}$.

B. Balancing Gait

Balancing gait extends Sliding gait by two additional weight-shifting phases, denoted *Shifting Back* and *Shifting Front*, which are performed to apply more load to the anchoring segment. Shifting back moves the *Center of Mass* (CoM) closer to the back segment by setting the supporting segment servo angle $\alpha_{\text{support}} = \alpha_{\text{support}}^{\text{balancing}}$ at the beginning of the extension phase, while shifting front moves the CoM closer to the front segment at the beginning of the contraction phase.

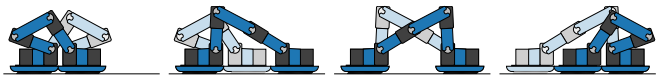

(a) Shift Back. (b) Extension. (c) Shift Front. (d) Contraction.

Fig. 3: Balancing gait phases for $l_{\text{min}}^{\text{balancing}} = 100\,\text{mm}$, $l_{\text{max}}^{\text{balancing}} = 200\,\text{mm}$, and $\alpha_{\text{support}}^{\text{balancing}} = 160°$.

C. Stepping Gait

Stepping gait builds upon Balancing gait by adding pad *up* and pad *down* phases for both front and back pads, exploiting the lower friction of the stiff bumpers compared to the soft friction pads. By adjusting the segment *Angle*

of Attack (AoA), the normal load is shifted onto the rigid borders to disengage the scales and facilitate a smoother sliding transition even if scales remain in partial contact. The angles $\alpha_{\text{front}} = \alpha_{\text{front}}^{\text{stepping}}$ and $\alpha_{\text{back}} = \alpha_{\text{back}}^{\text{stepping}} \triangleq \alpha_{\text{front}}^{\text{stepping}}$ are used to denote AoA of the front and back segment, respectively. The gait cycle is outlined in Fig. 4. Note that exploiting the friction differences between contact materials across multiple terrains [21] can be used to create a stepping gait that moves backwards.

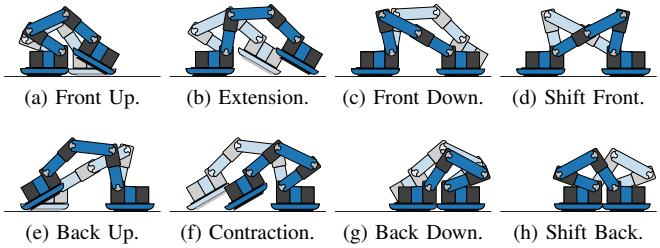

(a) Front Up. (b) Extension. (c) Front Down. (d) Shift Front.

(e) Back Up. (f) Contraction. (g) Back Down. (h) Shift Back.

Fig. 4: Stepping gait phases for $l_{\text{min}}^{\text{stepping}} = 100\,\text{mm}$, $l_{\text{max}}^{\text{stepping}} = 180\,\text{mm}$, $\alpha_{\text{support}}^{\text{stepping}} = 160°$, and $\alpha_{\text{front}}^{\text{stepping}} = \alpha_{\text{back}}^{\text{stepping}} = 30°$.

IV. Robot Design

The studied adaptive locomotion is motivated by an affordable inchworm-like robot with anisotropic frictional footpads [9]. While we adopt the core architecture for linear locomotion, we extend the platform to 2D maneuvers by incorporating two additional degrees of freedom (DoF) for steering. Implementing It requires structural modifications to the morphology (Section IV-A) and the addition of multidirectional anisotropic friction (Section IV-B) to implement it. An optical-sensor-based slip detection system is integrated into the contact segments to support gait adaptation (Section IV-C).

A. Proposed Inchworm Robot Body with Turning Capability

The mechanical design is an extension of the 1D prototype [9], with primary structural modification in the form of two active steering joints that rotate the friction pads to enable planar maneuvers. The proposed design uses Robotis Dynamixel XM430-W350-R servomotors and 3D-printed links made from Polyethylene Terephthalate Glycol (PETG). The design is illustrated in the render depicted in Fig. 5.

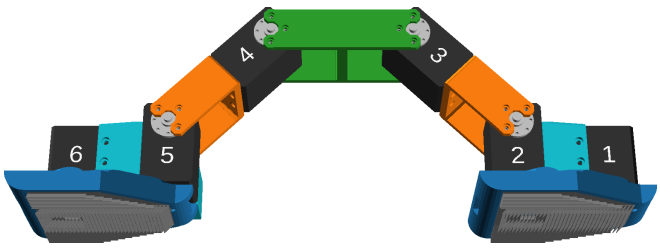

Fig. 5: Render of the robot architecture: six servomotors (black), 3D-printed PETG structural links (orange and green), multidirectional anisotropic friction pads (grey), and rigid low-friction bumpers (blue).

The actuators are numbered sequentially from 1 to 6 along the longitudinal axis. The four central servomotors (2–5) comprise the *core servomotors* as they are used for forward motion, while the outermost servomotors (1 and 6) engage mainly when turning. The detailed kinematic dimensions and body parameters are provided in Fig. 6 and Table I to facilitate reproducibility.

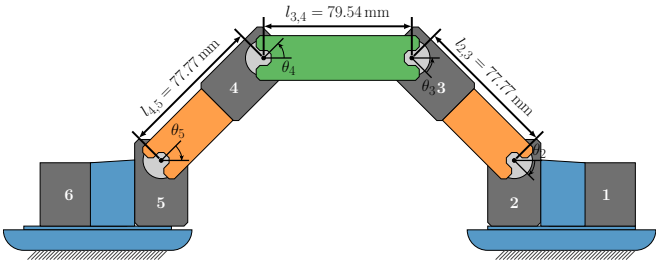

Fig. 6: The robot kinematics parameters.

The robot interacts with the environment through the *contact segments*, consisting of soft friction pads (see Section IV-B) and the stiff bumper framing. The core servomotors provide extension/contraction capabilities while keeping front and back contact segments at the given AoA using the 3 out of 4 DoF. The remaining servomotor enables load distribution among the contact segments by manipulating the CoM to increase the load (normal force) on the anchoring segment. Due to the robot construction with two pairs of servomotors situated close to the contact pad, the main way of manipulating the CoM is via positioning remaining servomotor 3 and 4 as close to the servomotor 1 and 6 as possible, respectively. The angle on the servomotor implementing CoM manipulation is referred to as α_{support}. The maximum value of $\alpha_{\text{support}}^{\text{max}}(l)$ is limited by the robot kinematics and decreases with increasing distance l between the contact pads, causing the CoM manipulation effect to vanish as the robot extends.

TABLE I: Kinematics Parameters

Link lengths [mm]			**Contact segment parameters** [mm]					
$l_{1,2}$	$l_{2,3}$	$l_{3,4}$	s_y	s_{f_f}	s_{f_b}	s_{b_f}	s_{b_b}	s_r
77.77	79.54	77.77	48.25	76.00	25.25	16.50	84.75	11.00

Joints Limits	θ_1	θ_2	θ_3	θ_4	θ_5	θ_6
min[°]	−45	0	0	0	0	−45
max[°]	45	160	140	140	160	45

B. Proposed Friction Pads for Multi-Directional Motion

The proposed friction pads replace the inchworm limbs as the means of anchoring to the terrain and consist of rows of flexible scales. A flexible *scales row* has a *preferred direction*, such as forward, where friction is assumed to be lower than *resisting direction*, such as backward. The scale layout and parameters are depicted in Fig. 7 with the preferred direction marked by a white arrow. Individual scales point in resisting direction; therefore, they can resist motion caused by scale flexing when engaging with a terrain as depicted in Fig. 8a.

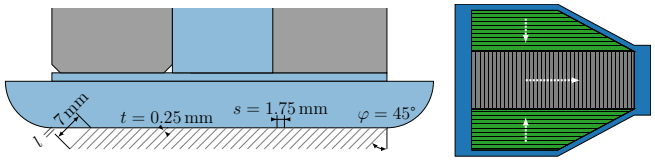

(a) Scales parameters (b) Scales division

Fig. 7: Scales have the length $l = 7\,\text{mm}$, thickness $t = 0.25\,\text{mm}$, angled at $\varphi = 45°$, and spaced at $s = 1.75\,\text{mm}$ for the middle longitudinal area (gray area on right) and of the length $l' = 5\,\text{mm}$ for the radial scales (green areas on the right). The white dashed arrow indicates the preferred direction of motion for the scales, with lower friction.

On the other hand, when the scales row moves in the preferred direction, the individual scales can bend toward the robot's abdomen without engaging with the terrain as depicted in Fig. 8b. Sufficient friction between the scale material and terrain is required for anisotropy to be pronounced, as examined in [21]. Moreover, increasing the normal force applied to the scales further increases the friction force; hence, enhancing the friction anisotropy.

Assuming the quasi-static stability, the relation between the maximum friction force at the front $\mathcal{F}_f^F$ and back $\mathcal{F}_b^F$ can be modeled based on the CoM projection r_{CoM_p}, relative to the front and back segment positions r_f and r_b as

$$\frac{\mathcal{F}_b^F}{\mathcal{F}_f^F} = \frac{\mu_b(0) \cdot \mathcal{F}_b^N}{\mu_f(0) \cdot \mathcal{F}_f^N} = \frac{\mu_b(0) \cdot (r_f - r_{CoM_p})}{\mu_f(0) \cdot (r_{CoM_p} - r_b)}, \quad (1)$$

where $\mu_f(0)$ and $\mu_b(0)$ denote forward and backward static friction coefficients, and $\mathcal{F}_f^N$ and $\mathcal{F}_b^N$ denote normal forces acting on the front and back segment, respectively. The gait is designed to manipulate the CoM such that $\mathcal{F}_b^F \gg \mathcal{F}_f^F$, ensuring the back segment effectively anchors the body during forward motion. For locomotion to proceed, the maximum static friction of the supporting segment must exceed the total resistive (dynamic) friction of the sliding segment.

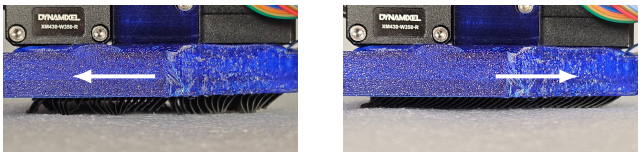

(a) Resisting backward direction (b) Preferred forward direction

Fig. 8: Scales' behavior under different motions applied.

The three different scales rows are proposed in friction pads to enable multidirectional motion: a single longitudinal (forward-backward) scales row engaging with the terrain during the forward motion, and two lateral (sideways) scales rows on the left and right side engaging when the robot is turning, as depicted in Fig. 7b. The longitudinal scales are $l = 7\,\text{mm}$ long, have thickness $t = 0.25\,\text{mm}$, are angled at $\varphi = 45°$, and are spaced $s = 1.75\,\text{mm}$ over the whole middle area such that the scales at the end of the pad can bend easily without interfering with the stiff bumpers as depicted in Fig. 7a. The radial scales are shorter $l' = 5\,\text{mm}$ and only engage when the robot is turning, but share other parameters with the longitudinal scales $t' = t$, $s' = s$, and $\varphi' = \varphi$. The scales are 3D-printed from FiberFlex 40D Thermoplastic Elastomer (TPE) filament by Fiberlogy using tabletop 3D printers. The printing is consistent with [9] that uses only longitudinal scales.

C. Slippage Sensors

Slippage occurs when the anchoring segment fails to resist the reaction forces generated during the opposing segment's motion. We propose detecting slippage using optical sensors embedded in the contact segment, as depicted in Fig. 9, to detect these events while maintaining a small footprint. We opted for an off-the-shelf low-power laser mouse sensor, the PMW3610DM-SUDU with LM18-LSI lens (Pixart Imaging), using Vertical-Cavity Surface-Emitting Laser (VCSEL) technology.

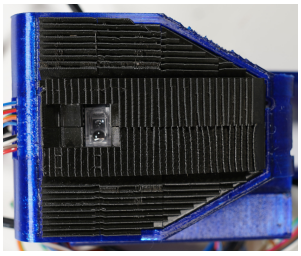

Fig. 9: Laser mouse sensor PMW3610DM-SUDU with LM18-LSI lens embedded in the contact segment.

The sensor's internal localization algorithm provides the relative XY-displacement and a *surface quality* metric representing the number of trackable features. While the displacement values are used for slip detection, the surface quality metric can identify sensor malfunctions or specular reflections. However, such analysis is beyond the scope of the presented work. Data acquisition is handled via an `SPI` interface, with an STM32F042K6 (Nucleo) microcontroller development board serving as an `SPI`-to-`USB` bridge. The configuration supports off-board processing, ensuring that the required computational overhead does not constrain the robot's physical design.

V. Proposed Control and Adaptive Locomotion

The proposed generalization of the inchworm-like robot, with its turning capabilities and adaptive locomotion, follows the original robot design and locomotion [9]. Their capabilities can be summarized as follows.

- The *Sliding gait* uses only the friction pad anisotropy to locomote via extension and contraction.
- The *Balancing gait* adds the CoM manipulation to Sliding gait for further improvement of frictional anisotropy.
- The *Stepping gait* extends the Balancing gait by using the stiff bumpers for locomotion.

The gaits have a given number of *gait phases* each with given duration τ and uses the robot state-space parameters consisting of distance between contacts points l, the front and back pad angle α_{front} and α_{back}, respectively, the front and back steering angle $\theta_{\text{front}} = \theta_1$ and $\theta_{\text{back}} = \theta_6$, and the support angle α_{support}. Therefore, we need to find a way to

adjust the gaits to exploit the enhanced inchworm's turning capability and to detect slippage and propagate a corrective action to the gait parameterization. The proposed solutions to address turning and gait adaptation are presented in the following paragraphs.

A. Steering Direction of the Locomotion

Steering is integrated into the gait cycle by introducing two additional phases: a *steering phase* immediately preceding the extension, and a *realigning phase* prior to contraction. During the steering phase, the front and back contact segments are rotated in opposite directions by an angle θ_{steering} relative to the longitudinal axis to dictate the robot's new heading. During the realigning phase, both segments return to the neutral zero position.

We adopt a discrete-step bicycle model to model 2D steering kinematics as

$$R = \frac{L}{\tan(\varphi)} = \frac{l_{\text{min}}}{\tan(2\,\theta_{\text{steering}})}, \tag{2}$$

where R is the predicted turning radius and $\varphi = 2\,\theta_{\text{steering}}$ represents the effective steering angle because both segments contribute to the change in orientation θ_{steering}. The characteristic wheelbase L is defined as l_{min}, since the robot is in its fully contracted state at the moment of steering. The model (2) accounts for the discrete nature of the inchworm's orientation changes, which occur primarily while the robot maintains its minimum internal displacement.

B. Gaits Adaptation

The basic idea of adaptive gait is to increase the load on the anchoring pad whenever slippage occurs. The slip event is important because we do not assume any prior knowledge of the terrain or its friction properties. The load increase is only possible by adjusting the robot's CoM to be closer to the anchoring pad. Based on the observation of the robot locomotion using the gaits from Section III, we propose the following way to estimate the needed adjustment to the gait parameterization that would yield the needed increase of the friction force.

During a gait cycle, the robot moves forward by about the *step length* $\Delta l = l_{\text{max}} - l_{\text{min}}$ assuming that the segment efficiently anchors the robot to the ground. Since changing the supporting segment and engaging and disengaging the scales takes some time, Δl should be maximized to increase the robot's average ideal speed $\hat{v}$. However, the control over the CoM decreases with increasing distance l_{max}, and it might result in slippage during the gait cycle and a decrease in true average speed v if the friction between pads and terrain is not sufficient.

For a single known terrain, l_{max} can be computed using known frictional properties, as shown in [21], tuning the gait parameters off-line [9]. For online adaptation of l_{max}, we further need slippage detection followed by gait parameters adaptation based on the observed displacement and current robot state.

The displacements can be measured during the contraction and extension phases, as these phases change the distance between the contact pads, thereby generating additional force on the segments. However, slippage may occur at any gait phase in both segments simultaneously. Namely, the back segment motion is measured during the extension phase, when the back segment is expected to anchor the robot to the ground, and the front segment motion is measured during contraction, when the roles are reversed.

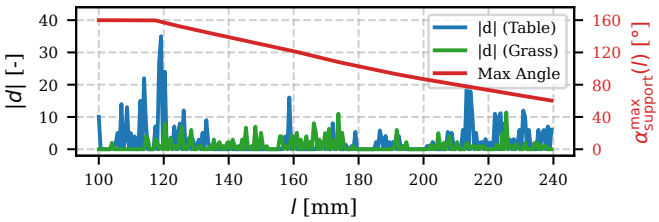

Fig. 10: Measured displacement magnitude $|d|$ for high-friction terrain (Grass in green) and low-friction terrain (Table in blue) for extending the distance l. The second y-axis shows the kinematics limits of $\alpha^{\text{max}}_{\text{support}}(l)$.

For a specific deployment, the measurements result in displacement sequences $\mathbf{d}$ with individual displacements $d_i = (d_{i_x}, d_{i_y})$ for both the front $\mathbf{d}_{\text{front}}$ and back $\mathbf{d}_{\text{back}}$ as illustrated in Fig. 10. The scales bend slightly as the robot engages the terrain before fully anchoring to the ground. The behavior results in displacement measured by the sensors, which does not constitute true slippage. We employ a magnitude threshold d_{thr} acting as a heuristic filter to distinguish between these elastic deformations and true slippage. In particular, $||d_i|| < d_{\text{thr}}$ are attributed to the sensor noise and pad bending and $||d_i|| \leq d_{\text{thr}}$ are classified as slippage.

There are two gait parameters suitable for gait adaptation: the supporting angle α_{support} and the maximum extension l_{max}. The maximum extension l_{max} is used for gait adaptation since it directly affects the maximum $\alpha^{\text{max}}_{\text{support}}(l)$ that can be reasonably controlled only for a short l, see Fig. 10. We propose to immediately terminate the extension phase and transition to the following gait phase, effectively decreasing l_{max} to adapt the gait parameters to the slippage detection.

Using the proposed slippage detection reaction policy allows the gait to adapt instantaneously to a new terrain, regardless of the frictional quality compared to the current terrain. Note that the gait adaptation is not possible for Sliding gait as it lacks the means to affect the CoM. Compared to [9], Sliding and Stepping gait uses maximum support angle $\alpha^{\text{max}}_{\text{support}}(l)$ depicted red in Fig. 10 if maintaining the desired α_{support} is not possible for the current length l.

VI. Experimental Results

The proposed adaptive, friction-anisotropy-based locomotion has been experimentally validated using the real robot developed and four terrain types in the experimental setup depicted in Fig. 11. The evaluation is focused on adaptation locomotion, while the feasibility of the proposed steering mechanism has been experimentally verified in a simple test (see Section VI-B) and further demonstrated in the accompanying video.

Fig. 11: Snapshots of the experimental setup used for evaluation of the developed adaptive locomotion on the Grass and Table terrains.

The test terrains include *Expanded Polyethylene* (EPE), artificial *Grass*, *Polyethylene Terephthalate Glycol* (PETG), and *Table*. The $5\,\mathrm{mm}$ thick EPE sheet is assumed to offer adequate friction for the pad, while Grass (with stems approximately $5\,\mathrm{mm}$ long and $1.5\,\mathrm{mm}$ wide) is anticipated to provide sufficient directional friction. The glossy PETG tiles, with sub-millimeter grooves (about $0.2\,\mathrm{mm}$ wide), are expected to offer challenging, low-friction, low-optical-quality terrain. The smooth mate table desk (denoted Table) is expected to provide low friction and sufficient quality for the optical sensor.

The benefit of the proposed adaptive locomotion is compared with the offline-tuned gaits for each terrain. For both options, the control frequency has been set to $f_c = 100\,\mathrm{Hz}$ with the servomotor communication at $2\,\mathrm{Mbit\,s^{-1}}$ and optical sensor communication at $1\,\mathrm{Mbit\,s^{-1}}$ for each gait to unify the testing conditions. The servomotors are current-controlled with PID, and the position and current i measurements are collected every $dt = 10\,\mathrm{ms}$. The optical mouse sensor is collected at the same rate and set to 1200 CPI (Counts Per Inch). The detection threshold $d_{\mathrm{thr}} = 20\,\mathrm{ticks} = 0.42\,\mathrm{mm}$ was observed to filter out the sensor noise and scales' elastic deformations when engaging with terrain.

TABLE II: Offline Tuned Gait Parameters

	l_{max}[mm]			
Gait Type	**EPE (E)**	**Grass (G)**	**PETG (P)**	**Table (T)**
Balancing Gait	240	240	190	150
Stepping Gait	206	199	210	210

Sliding gait parameterization does not allow adaptation, and therefore, only the fixed maximum length $l_{\mathrm{max}}^{\mathrm{sliding}} = 280\,\mathrm{cm}$ is used for a single universal (U) sliding gait configuration employed for all the evaluation terrains. The minimum gait length $l_{\mathrm{min}} = 100\,\mathrm{mm}$ is used for all gaits to ensure reliable clearance between the front and back segments. The identified static values of l_{max} for Balancing and Stepping gaits on each terrain type are depicted in Table II.

Both Balancing gait and Stepping gait are parameterized for each of four specific terrains in addition to the proposed adaptive locomotion. We encode the gait parameterization using a single letter as follows.

- **E** – Tuned parameterization for the EPE terrain.
- **G** – Tuned parameterization for the Grass terrain.
- **P** – Tuned parameterization for the PETG terrain.
- **T** – Tuned parameterization for the Table terrain.
- **A** – The proposed adaptive locomotion control.

The locomotion gaits are deployed on four flat terrains and run for 10 gait cycles. The performance of the locomotion control is measured by three performance indicators.

- The **average speed** v is computed from the measured traveled distance $\mathcal{L}$ and known gait cycle duration $\mathcal{T}$.
- The **Cost of Transport** (CoT) is computed from measured traveled distance $\mathcal{L}$, measured currents i and known voltage $u = 12\,\mathrm{V}$ as $\mathrm{CoT} \triangleq \frac{u}{\mathcal{L}} \sum (i \cdot dt)$.
- The **traveled distance efficiency** $\mathcal{L}_{\mathrm{eff}}$ is computed as the ratio of the measured distance $\mathcal{L}$ and the sum of the expected gait cycle steps under ideal conditions $\mathcal{L}_{\mathrm{ideal}}$.

Note that v and CoT focus on the absolute performance of individual gaits' parameterization, and $\mathcal{L}_{\mathrm{eff}}$ provides insight into execution reliability. Moreover, since the difference between expected gait cycle duration and real duration is negligible, the velocity efficiency v_{eff} has the same value as traveled distance efficiency $\mathcal{L}_{\mathrm{eff}}$.

A. Performance of Locomotion Control Strategies

All three locomotion gaits: *Sliding Gait*, *Balancing Gait*, and *Stepping Gait* have been deployed in all four terrain types. The *Sliding Gait* does not allow adjustment, and therefore only its single universal parameterization U has been deployed. On the other hand, *Balancing Gait* and *Stepping Gait* have been tuned for each specific terrain (see Table II), with the parameterization denoted E, G, P, and T, in addition to the proposed adaptive locomotion control denoted A. Then, each gait parameterization has been deployed in each terrain, yielding an evaluation matrix for each of the four performance metrics. The performance results are depicted in Fig. 12 and Fig. 13.

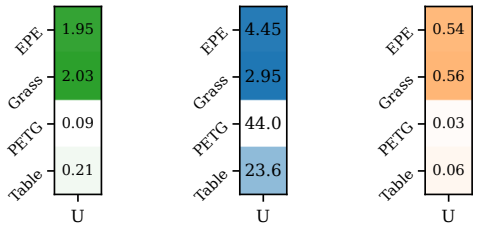

(a) v (b) CoT (c) $\mathcal{L}_{\mathrm{eff}}$

Fig. 12: The **Sliding Gait** evaluation metrics average velocity v $[cm/s]$, CoT $[J/cm]$, and traveled distance efficiency $\mathcal{L}_{\mathrm{eff}}$ $[-]$ for tested terrains (rows). A higher color intensity in the cell indicates better performance.

The ***Sliding Gait*** is deployed only with the single universal parameterization, denoted U, as it does not allow adjustment of the parameterizations. However, the single parameterization U outperforms the other gaits for terrains with sufficient friction (EPE and Grass), but fails for terrains with low friction (PETG and Table), as depicted in Fig. 12. These results show the importance of CoM manipulation, even at the cost of decreased performance, under ideal conditions.

Balancing Gait evaluation, depicted left in Fig. 13, suggests that the adaptive locomotion (A) achieves similar performance to Balancing gait tuned for a specific terrain. Specifically for the average speed and CoT, the worst performance of the adaptive locomotion (A) was achieved for

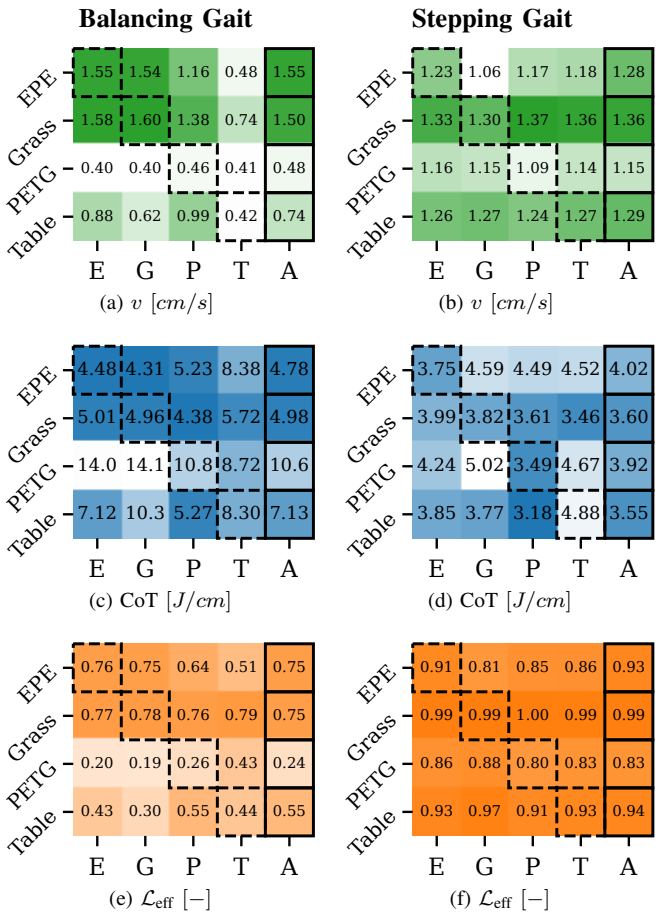

Fig. 13: The **Balancing Gait** (left column) and the **Stepping Gait** (right column) evaluation metrics for tested terrains using static parameterizations (E, G, P, T) and adaptive parameterization (A). A higher color intensity in the cell indicates better performance. The dashed cells denote the benchmark results where parameterization matches the terrain. The solid rectangle highlights our proposed method.

CoT on the EPE, where adaptive gait achieved 94 % of the gait tuned for EPE. On the other hand, the adaptive gait outperformed the table-specific gait CoT by 14 %, its speed by 76 %, and travel distance efficiency by 24 %. We attribute this significant improvement to adaptive gait's ability to fine-tune gate parameters in real time, accounting for phenomena that are difficult to capture during static offline tuning. The data also suggest that gaits tuned to terrains with sufficient friction (EPE and Grass) perform comparably well on other high-friction terrains. The adaptive gait performed with 75 % reliability for the high-friction terrain, but was outperformed by the table-tuned gait on the PETG terrain. We hypothesize that the repetitive sub-millimeter structure of 3D-printed PETG induces tracking errors despite high surface quality. Future work could explore fusing redundant optical sensors per pad or integrating optical data with motor measurements (position and velocity) and on-board IMU measurements through Kalman filtering to improve reliability.

Stepping Gait evaluation depicted right in Fig. 13 suggests that adaptive gait achieves similar performance to other parameterizations. The results are less pronounced, especially for the *traveled distance efficiency* $\mathcal{L}_{\text{eff}}$, since the combination of the contact materials in Stepping Gait provides a robust way of traversing the terrain with a low effect of particular frictional properties. Regarding velocity and distance efficiency, the adaptive gait outperforms or matches the performance of the gaits tuned to the particular terrain, as indicated by the maximum value in column A per row. As of CoT, the adaptive gait achieves 88 % of the PETG-tuned gait but outperforms the table-tuned gait by 27 %.

B. Turning Gait Extension

The steering capabilities of the proposed 2D locomotion were evaluated on two surfaces: artificial grass (high friction) and a smooth table surface (low friction). Segment positions were tracked using the PTI Phoenix VZK10K active 3D motion capture system at $f_{\text{PTI}} \approx 45\,\text{Hz}$. Sliding, Balancing, and Stepping gaits were tasked with executing three gait cycles with a steering command of $\theta_{\text{steering}} = 30°$. All gaits have increased $l_{\text{min}} = 110\,\text{mm}$ to enable collision-free pad rotations.

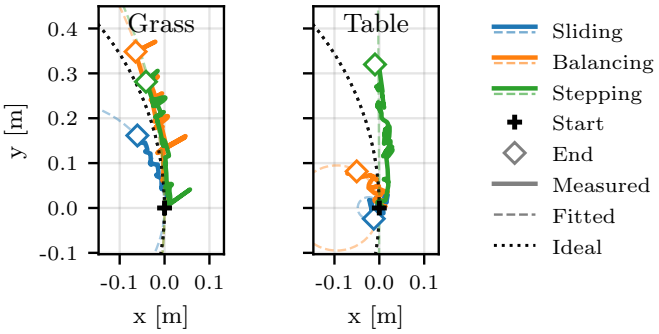

Fig. 14: Projected trajectories of the robot's midpoint for terrain-adapted gaits on Grass and Table. Solid lines represent measured trajectories, dashed lines show the fitted circles (R_{fit}), and dotted lines represent the kinematic model (2) under ideal conditions (R_{id}). Plus symbols denote origins, and diamonds mark the color-coded end positions.

The 3D marker data were projected onto the motion plane using a stationary reference triplet. The robot's trajectory was defined by the midpoint between the front and back segment centers. These points were smoothed using a third-order Savitzky-Golay filter (window size of 21 samples, $\approx 0.5\,\text{s}$) and a circle was fitted to the resulting path, as shown in Fig. 14.

TABLE III: Turning Radius and Heading Evaluation

Terrain	**Gait**	R_{fit} **[m]**	E_R **[-]**	$\Delta\phi$ **[°]**	E_ϕ **[-]**	$\mathcal{L}_{\text{eff}}$ **[-]**
Grass	Sliding	0.24	-0.62	15.13°	0.83	0.29
	Balancing	1.06	0.67	19.27°	0.79	0.67
	Stepping	1.15	0.81	21.75°	0.76	0.81
Table	Sliding	—	—	15.02°	0.83	0.02
	Balancing	—	—	68.06°	0.24	0.20
	Stepping	1865	2936	14.06°	0.84	0.29

The quantitative results in Table III demonstrate that while the robot effectively navigates high-friction surfaces, performance degrades on low-friction terrains. On artificial

grass, the robot followed the predicted turning radius with reasonable accuracy, despite a heading error $\Delta\phi$. On the table surface, lateral slippage was significantly more pronounced than in forward locomotion; the Sliding gait struggled to achieve any meaningful displacement; the Balancing gait's forward motion was severely limited; and the Stepping gait moved forward but failed to execute the turn.

Distance efficiency $\mathcal{L}_{\text{eff}}$ decreased significantly during turning by up to $60\,\%$ on Table and $45\,\%$ on Grass compared to the same terrains in forward-motion only scenarios. We hypothesize that changing the pad angle affects the longitudinal scales' efficiency and decreases anchoring quality, thereby reducing the ability to follow the expected trajectory accurately.

VII. Conclusion

In the presented paper, we address adaptive locomotion of an inchworm-like robot using anisotropic friction. We leverage prior work and generalize the robot design to enable directional control. However, the key property of the developed locomotion control is that it does not rely on the offline tuning of the gait parameters. The proposed adaptive locomotion is based on slippage detection using the off-the-shelf optical mouse sensors. The robot's locomotion performance is experimentally evaluated using previously developed locomotion gait controllers tuned for specific terrains. Two of the gaits utilize the frictional anisotropy solely, while others combine the anisotropy with the hard bumper material. The experimental results indicate that employing adaptive locomotion improves the overall gait performance, even when the gaits are explicitly tuned to a particular terrain. The scale of improvement depends on gait robustness. Since the experimental data suggest that there are energy-efficient gaits for specific terrain properties, future work could focus on gait switching or online gait learning.

Acknowledgments

The authors would like to thank M. Škarytka for the optical sensor printed circuit board design and assembly, and K. Kubíková for providing the real inchworm photography.

References

[1] C. Tiner, S. Bapat, S. D. Nath, S. V. Atre, and A. Malshe, "Exploring convergence of snake-skin-inspired texture designs and additive manufacturing for mechanical traction," *Procedia Manufacturing*, vol. 34, pp. 640–646, 2019. doi: 10.1016/j.promfg.2019.06.116

[2] M. B. Khan, T. Chuthong, C. Danh Do, M. Thor, P. Billeschou, J. C. Larsen, and P. Manoonpong, "iCrawl: An inchworm-inspired crawling robot," *IEEE Access*, vol. 8, pp. 200 655–200 668, 2020. doi: 10.1109/ACCESS.2020.3035871

[3] R. Li, Y. Liu, A. Guo, M. Shou, M. Zhao, D. Zhu, P.-a. Yang, and C.-H. Lee, "An inchworm-like climbing robot based on cable-driven grippers," *IEEE/ASME Transactions on Mechatronics*, pp. 1–10, 2023. doi: 10.1109/TMECH.2023.3307682

[4] Y. Zhou and Q. Zeng, "Inchworm robot structural design and kinematic modeling," in *International Conference on Computing, Robotics and System Sciences (ICRSS)*, 2022, pp. 1–5. doi: 10.1109/ICRSS57469.2022.00011

[5] W. Saab, A. Kumar, and P. Ben-Tzvi, "Design and analysis of a miniature modular inchworm robot," in *International Design Engineering Technical Conferences and Computers and Information in Engineering Conference*, 2016. doi: 10.1115/DETC2016-59386

[6] T. Duggan, L. Horowitz, A. Ulug, E. Baker, and K. Petersen, "Inchworm-inspired locomotion in untethered soft robots," in *IEEE International Conference on Soft Robotics (RoboSoft)*, 2019, pp. 200–205. doi: 10.1109/ROBOSOFT.2019.8722716

[7] B. Gamus, L. Salem, A. D. Gat, and Y. Or, "Understanding inchworm crawling for soft-robotics," *IEEE Robotics and Automation Letters*, vol. 5, no. 2, pp. 1397–1404, 2020. doi: 10.1109/LRA.2020.2966407

[8] B. Gamus, A. D. Gat, and Y. Or, "Dynamic inchworm crawling: Performance analysis and optimization of a three-link robot," *IEEE Robotics and Automation Letters*, vol. 6, no. 1, pp. 111–118, 2021. doi: 10.1109/LRA.2020.3033258

[9] J. Kubík, A. Rišková, and J. Faigl, "Inchworm-like robot locomotion using off-the-shelf 3d-printable anisotropic friction pads," in *The 12th International Symposium on Adaptive Motion of Animals and Machines (AMAM) and 2nd LokoAssist Symposium*, 2025. doi: 10.26083/tuprints-00030958

[10] M. Focchi, V. Barasuol, M. Frigerio, D. G. Caldwell, and C. Semini, "Slip detection and recovery for quadruped robots," in *Robotics Research: Volume 2*, 2018, pp. 185–199. doi: 10.1007/978-3-319-60916-4_11

[11] Z. Yoon, J.-H. Kim, and H.-W. Park, "Invariant smoother for legged robot state estimation with dynamic contact event information," *IEEE Transactions on Robotics*, pp. 193–212, 2024. doi: 10.1109/TRO.2023.3328202

[12] J. Yang, K. Hirashima, S. Taylor, T. Seo, and J. Kim, "State estimation for 2-legged robots using foot slippage and body impact detection," in *International Conference on Ubiquitous Robots (UR)*, 2025, pp. 1–7. doi: 10.1109/UR65550.2025.11078053

[13] R. A. Romeo and L. Zollo, "Methods and sensors for slip detection in robotics: A survey," *IEEE Access*, vol. 8, pp. 200 655–200 668, 2020. doi: 10.1109/ACCESS.2020.2987849

[14] A. Cavallo, G. De Maria, C. Natale, and S. Pirozzi, "Slipping detection and avoidance based on kalman filter," *Mechatronics*, vol. 24, no. 5, pp. 489–499, 2014. doi: 10.1016/j.mechatronics.2014.05.006

[15] M. Stachowsky, T. Hummel, M. Moussa, and H. A. Abdullah, "A slip detection and correction strategy for precision robot grasping," *IEEE/ASME Transactions on Mechatronics*, vol. 21, no. 5, pp. 2214–2226, 2016. doi: 10.1109/TMECH.2016.2551557

[16] J.-K. Lee, H.-H. Kim, J.-W. Choi, K.-C. Lee, and S. Lee, "Development of Direct-printed Tactile Sensors for Gripper Control through Contact and Slip Detection," *International Journal of Control, Automation and Systems*, vol. 16, pp. 929–936, 2018. doi: 10.1007/s12555-017-0151-x

[17] W. Yuan, R. Li, M. A. Srinivasan, and E. H. Adelson, "Measurement of shear and slip with a gelsight tactile sensor," in *IEEE International Conference on Robotics and Automation (ICRA)*, 2015, pp. 304–311. doi: 10.1109/ICRA.2015.7139016

[18] J. W. James, N. Pestell, and N. F. Lepora, "Slip detection with a biomimetic tactile sensor," *IEEE Robotics and Automation Letters*, vol. 3, no. 4, pp. 3340–3346, 2018. doi: 10.1109/LRA.2018.2852797

[19] A. Maldonado, H. Alvarez, and M. Beetz, "Improving robot manipulation through fingertip perception," in *IEEE/RSJ International Conference on Intelligent Robots and Systems (IROS)*, 2012, pp. 2947–2954. doi: 10.1109/IROS.2012.6385560

[20] D.-H. Yi, T.-J. Lee, and D.-I. Dan" Cho, "Afocal optical flow sensor for mobile robot odometry," in *International Conference on Control, Automation and Systems (ICCAS)*, 2015, pp. 1393–1397. doi: 10.1109/ICCAS.2015.7364858

[21] A. Rišková, J. Kubík, and J. Faigl, "Automated evaluation of anisotropic friction pads," in *The 12th International Symposium on Adaptive Motion of Animals and Machines (AMAM) and 2nd LokoAssist Symposium*, 2025. doi: 10.26083/tuprints-00030932